



A novel numerical modeling of microsecond laser beam percussion micro-drilling of Hastelloy X: experimental validation and multi-objective optimization

Milad Aghaei Attar¹ · Omid Razmkhah² · Majid Ghoreishi¹ · Mahmoud Moradi³

Received: 21 June 2023 / Accepted: 28 December 2023 / Published online: 8 March 2024
© The Author(s) 2024

Abstract

The paper investigates the characteristics of the laser beam percussion micro-drilling (LBPM) process in aerospace nickel-based superalloy Hastelloy X using microsecond pulses. The quality of the drilled hole is crucial in laser beam micromachining, and selecting appropriate process parameters significantly impacts the hole's quality. The objective is to achieve predefined hole dimensions with minimal taper angles. Additionally, the study focuses on the alteration of pulse width, which is a combination of laser pulse frequency and duty cycle. Laser power (P), duty cycle % (D), focal plane position (FPP), and laser frequency (f) are considered input parameters, while geometric features such as inlet and outlet diameters, hole taper angle, and inlet circularity are examined as process responses. ANOVA is employed to establish significant relationships between process parameters and response variations based on experimental tests. Creating a precise simulation model that accurately accounts for the moving boundary of the target material's receding surface is a crucial and challenging task in formulating the laser heat conduction problem. It is necessary to simultaneously capture the material's dynamic front movement and update the boundary conditions of the laser source. To model the micro-drilled hole with LBPM, the UMESHMOTION and DFLUX subroutines, along with the arbitrary Lagrangian-Eulerian (ALE) adaptive remesh algorithm in the AbaqusTM software, are utilized. Notably, no previous numerical study has predicted the geometry of micro-drilled holes using this technique. The proposed procedure is validated through the predictions of inlet and outlet hole diameters. Special emphasis is placed on the validation of models. Consequently, the numerical model and statistical model are compared as well as the need to define model applicability. The study demonstrates that all input parameters significantly influence the inlet hole diameter, while the pulse width notably affects the taper angle and circularity. The interaction between high laser frequency and low duty cycle results in reduced pulse duration. Multi-objective optimization is performed to determine the optimal process parameter settings for desired quality characteristics, considering minimum hole taper angle, precise inlet diameter, and maximum inlet circularity of the hole as optimization criteria. The findings show that with the optimized predicted results obtained from the optimal input variables, a composite desirability of 92% can be achieved.

Keywords LBPM (laser beam percussion micro-drilling) · Finite element method · Hastelloy X · Moving boundary condition · Response surface methodology (RSM)

✉ Mahmoud Moradi
Mohamoud.moradi@northampton.ac.uk

- ¹ Department of Mechanical Engineering, Faculty of Engineering, K. N. Toosi University of Technology, Tehran, Iran
- ² School of Mechanical, Aerospace and Automotive Engineering, Faculty of Engineering, Environment and Computing, Coventry University, Gulson Road, Coventry CV1 2JH, UK
- ³ Faculty of Arts, Science and Technology, University of Northampton, Northampton NN1 5PH, UK

1 Introduction

Laser material processing has emerged as a new method for achieving micro-hole drilling in hard-to-cut materials, thanks to its ultrafast and pulsed wave capabilities. It offers competitive features such as noncontact operation, high aspect ratio, high energy, and high efficiency. This method finds diverse applications in aerospace, medical implants, micro-electromechanical systems (MEMS), drug delivery orifices, electronic communications, energy batteries, and micro-optical artificial compound

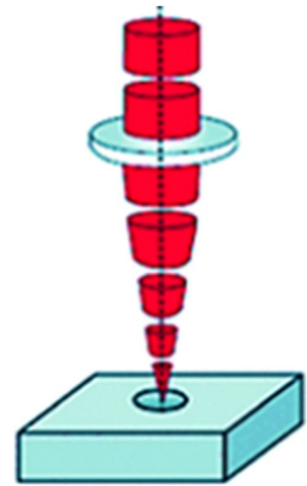
eyes [1, 2]. For example, laser micro-deep-hole drilling has been used by developers of surgical tools for the brain and bone to work with challenging metals like stainless steel and Ti6Al4V [3]. Similarly, micro-holes in turbine blades serve as cooling channels in the aviation sector.

In this study, Hastelloy X is chosen as the target material. It is a nickel-based superalloy with a high iron content, solid-solution-strengthened with Cr-Mo. Hastelloy X is widely recognized as a difficult-to-machine or high-tech material due to its high working temperatures, high creep resistance, excellent oxidation resistance, remarkable hardness, and low thermal conductivity [4]. Consequently, it is extensively used in manufacturing high-temperature components for aerospace applications, including jet engine tailpipes, nozzle vanes, afterburner components, turbine blades, combustion chamber components, and other aircraft parts [5, 6].

However, the laser micro-drilling process faces certain limitations. Achieving a low hole taper angle, minimizing the heat-affected zone (HAZ), ensuring high circularity and a high aspect ratio, and minimizing recast formations and other metallurgical defects pose challenges [7]. These issues are more prevalent in stationary beam drilling techniques like percussion drilling compared to moving beam methods such as trepanning and helical drilling [8, 9]. Nonetheless, achieving high-quality holes with maximum circularity, minimal difference between entrance and exit hole diameters, and low taper angles remains a requirement [10]. To attain high-quality holes, new methods and tools have been proposed, including changing the focal position, beam movement, underwater drilling [11], new drilling cycles [12], and the use of assist gas [13]. Several researchers have also developed processing parameters to achieve optimum responses with high quality.

In 2018, Moradi and Abdollahi conducted a study on statistical modeling and optimization of laser percussion micro-drilling in thin AMS 5510 stainless steel 321 sheets. They investigated the impact of varying laser beam frequency, duty cycle, and laser power as input parameters on hole geometry. The output factors analyzed included entrance and exit hole diameters, circularity, and taper angle. Their findings revealed a decrease in entrance hole diameter and taper

Fig. 1 Schematic figure of laser percussion drilling [22]



angle accordingly [14]. In 2021, Saravanan et al. optimized laser drilling parameters for creating holes in thin Ti6Al4V sheets. Laser power, laser speed, and laser pulse frequency were adjusted as input parameters to enhance hole circularity. Their study identified laser speed and frequency as the most significant factors influencing the process.

In conclusion, it was reported that hole circularity increases with increasing frequency and speed [15]. In 2021, Liu et al. investigated the feasibility of laser trepan drilling in a 2.5D Cf/SiC composite to create micro-holes. They found that the taper angle and heat-affected zone posed challenges during drilling. Their study concluded that defocusing had an extreme effect on the taper angle with a 75.42% contribution, while its effect on HAZ was negligible [16]. In 2018, Nasrollahi et al. used ultra-short pulsed laser for micro-drilling ceramic substrates and examined the impact of fluence and focal distance as input parameters. Their objective was to achieve high-aspect ratio holes and improve hole morphology and quality. They successfully controlled the taper angle and circularity to enhance hole quality by increasing fluence and decreasing the focal distance while considering the risk of recast formation [17]. Moradi and Golchin simulated the laser percussion micro-drilling process of nickel-based superalloy Inconel 718 in 2017 using the finite element method. They investigated laser pulse frequency, power, focal position, and duty cycle as input parameters. Increasing each input factor led to an increase in output parameters such as entrance and exit hole diameters, hole taper angle, and removal mass weight [18]. Arrizubietta et al. studied hole formation in laser percussion drilling of AISI 304 stainless steel plate with a thickness of 1 mm using a fiber laser. They achieved a taper angle of 2–4° at the entrance and exit of the hole, respectively. Panda et al. optimized the laser drilling process of stainless steel using the GRA (gray

Table 1 Designed levels of input variables of LBPM D

Variable	Symbol	Unit	-1	0	1
Laser power	P	W	500	600	700
Laser pulse frequency	f	Hz	1000	10,000	20,000
Focal plane position	FPP	mm	8	10	12
Duty cycle (pulse duration)	D	%	40	50	60

Table 2 Chemical composition (wt%) of Hastelloy X

Cr	Fe	Mo	Co	W	Mn	Si	Cu
21.27	18.63	8.59	1.55	0.59	0.51	0.24	0.24
Al	Nb	C	P	Ti	B	S	Ni
0.12	0.10	0.07	0.014	0.01	0.002	0.001	48.17

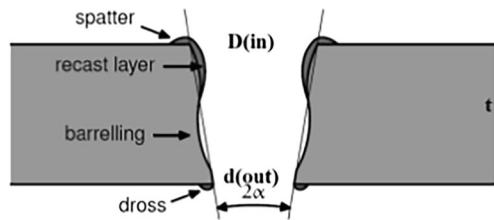


Fig. 2 Schematic of drilled geometry

relational analysis) approach and proposed optimal input parameters such as pulse width, number of pulses, assist gas flow rate, and gas pressure based on high quality in HAZ, hole diameter, and material removal rate [19]. In 2020, Zhao et al. examined the influence of high frequency on the geometry and morphology of micro-holes drilled in metals. They increased laser ablation efficiency with a high repetition rate, resulting in reduced ejection time of ablated material and cooling time of the substrate material. Their study reported the relationship between repetition rate, depth, and diameter of holes and found that the repetition rate had a weak or no effect on hole dimensions in micro-deep hole drilling [20].

In the present study, RSM (response surface methodology) was used to investigate the laser parameters on hole geometry in laser percussion micro-drilling. The geometry and morphology of the holes were analyzed in detail using a high-resolution optical microscope. To the best

of the authors’ knowledge, no previous study has numerically investigated laser percussion micro-hole drilling of Hastelloy X, accurately predicted hole dimensions, and solved the temperature field simultaneously. The modeling of laser percussion micro-drilling was performed using the DFLUX subroutine and UMESHMOTION combined with the arbitrary Lagrangian-Eulerian (ALE) adaptive mesh algorithm in the Abaqus™ software. The proposed model takes into consideration the temperature-dependent material and optical characteristics of the workpiece, as well as the percussion impact of the pulsed laser. The predicted geometrical and dimensional properties show superior agreement with experimental data compared to standard approaches in the literature. The model was validated by comparing the findings with experimental data. As a result, the experimental findings were optimized using multi-objective optimization based on Derringer’s technique to establish the ideal outputs and determine the effect of each input parameter.

2 Design of experiments and methodology

In the current study, the response surface methodology is used as the method for designing the experiment. The response surface approach is a method for determining the relationships between the input parameters of the process and the output responses [21]. There are several important criteria in the laser beam percussion micro-drilling (LBPM) process. In this study, the independent input variables selected were laser power (P), duty cycle (D), focal plane position (FPP), and laser frequency (f). The coded and actual values of the three input parameters are presented in Table 1. It is important to note that 31 trial specimens of laser percussion drilling were used by varying one of the process variables to determine the operating range of each parameter. Therefore, each of the input parameters was selected at three different levels, resulting in a total of 26 experiments conducted, 16 as cube points, eight as axial points in the cubic vertex, and two points in the cubic center. Table 1 illustrates the cubic space with design levels (−1 to +1) for the five varied parameters, according to the design matrix. The output parameters measured were inlet hole diameter, outlet hole diameter, taper angle, and inlet circularity of the drilled samples. Figure 1 illustrates the schematic diagram of laser percussion drilling.

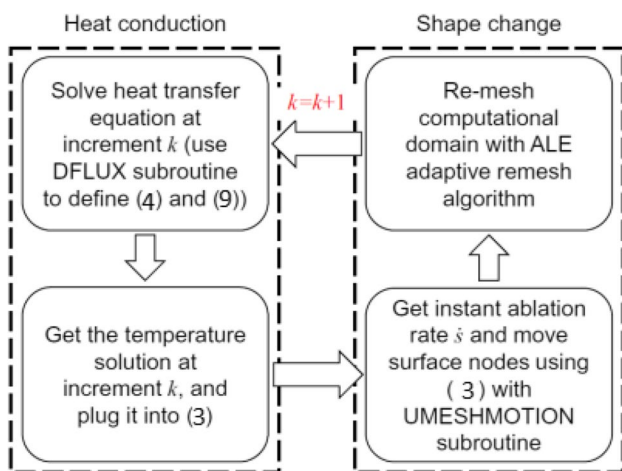


Fig. 3 Numerical modeling workflow of this study

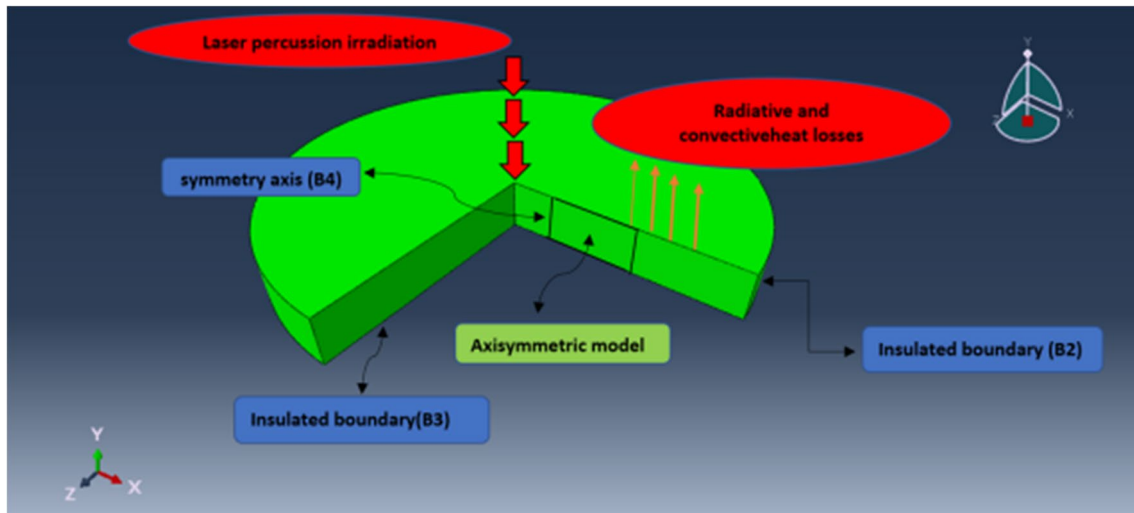


Fig. 4 Boundary conditions

3 Materials and methods

3.1 Material specifications

The thin sheet aerospace nickel-based superalloy Hastelloy X with a thickness of 1 mm was used as an experimental material workpiece. The chemical composition of the material, which is the average of three measurements, is reported in Table 2.

3.2 Laser processing procedure

For the LBPM process, a 1-kW fiber laser (YFL_1000_MM; model made in the Iranian National Laser Center) with a maximum average power of 1 kW, a nozzle diameter of 0.35 mm, the minimum spot size of the laser at a focal position of 200 μm , a focal length of 200 mm, and wavelengths of 1080 nm was used in pulsed mode [23]. In all trials, the argon assist gas pressure was employed with a gas flow rate of 15 L/min.

3.3 Experimental work

Laser drilling experiments were performed according to the matrix scheme of design of experiments (DOE) presented in Table 1. As previously stated, the output responses were inlet and outlet hole diameters, hole taper angle, and inlet circularity. Each parameter's measurement technique is detailed below. The output responses on the schematic drilled geometry are shown in Fig. 2.

3.3.1 Inlet and outlet hole diameters

The geometrical characteristics of the inlet and outlet hole diameters were recorded using an optical microscope (Axioskop 40; Carl Zeiss AG) at a magnification of $\times 940$.

Table 3 Temperature-dependent properties [30]

Temperature (K)	Density (kg/m^3)	Thermal conductivity (W/m K)	Specific heat (J/kg K)
298	8240	9.2	486
373	8221	11.2	487
473	8193	14.1	484
573	8162	15	491
673	8130	16.9	507
773	8095	18.8	531
873	8058	20.9	564
973	8019	22.8	606
1073	7978	24.7	657
1173	7934	26.7	716
1273	7889	28	784
1373	7841	30.2	860
1473	7792	32.4	936
1528	7761	33.7	936
1628	7420	30	936
1673	7363	30	936
1737	7280	30	936

Table 4 Absorptivity properties of Hastelloy X

Definition	Values
Permittivity of vacuum (C ² /N m ²)	8.85 × 10 ⁻¹²
Coefficient of resistance (1/K)	0.006
Conductance (Ω ⁻¹ m ⁻¹)	8.7 × 10 ⁵

Measurements of the inlet and outlet diameters and circularity of each hole were performed by the Visilog software [24]. The sizes of the inlet and outlet holes were regarded the primary factors, and additional criteria such as inlet circularity and hole taper angle were evaluated based on them.

3.3.2 Hole taper angle

Based on the inlet and outlet diameters, the hole taper is defined by Eq. 1:

$$\text{Taper angle}(\text{°}) = \text{ATAN} \left(\frac{D_{\text{entrance}} - D_{\text{exit}}}{2t} \right) \times \frac{180}{\pi} \quad (1)$$

where D_{entrance} is the inlet hole diameter, D_{exit} is the outlet hole diameter, and t is the thickness of the material.

3.3.3 Inlet circularity

Due to the ejection way of the molten material from the exit hole, outlet circularity is not a problematic parameter. Therefore, the hole exit is usually more circular than the hole entrance. However, different input variables affect the inlet circularity. The inlet circularity for the entire set of the experiments is conducted by measuring the hole diameter in an interval of 30° each along the circumference of the hole using a microscopic image and averaging the result using Eq. 2:

$$\text{Circularity}(C) = (D_{\text{min}}/D_{\text{max}}) \quad (2)$$

A hole circularity equal to 1.0 (100%) indicates that the hole is totally circular. D_{min} and D_{max} in Eq. 2 are the minimum and maximum hole diameters, respectively [25].

4 Numerical modeling

Finite element analysis (FEA) of microsecond LBPM is performed using Abaqus. The modeling implementation includes two basic subroutines: DFLUX and UMESHMOTION. The DFLUX subroutine allows us to model the pulsed laser heat source and account for heat loss due to convection and radiation [26]. It is important to note that special attention is required in the DFLUX subroutine to define the body heat flux, as the coordinate Z' ($Z' = Z - d$) moves with the progressive recession of

the target material’s surface. Thus, the coordinate Z' is updated after each time increment to reflect the current position.

$$Z^{(k+1)} = Z^{(k)} - s\Delta t \quad (3)$$

where k , with $k = 0, 1, 2, \dots$, is the increment number; s is the ablation rate; and Δt is the time increment. The time increment is 0.001. The ablation depth of the material during drilling results from the ablation rate and the time increment. Progressive variation of the surface during laser drilling to accurately predict the dimensions of the drilled hole is performed by the UMESHMOTION subroutine, in combination with the ALE adaptive mesh algorithm [27]. Specifically, the UMESHMOTION subroutine requires the temperature of each node to eval-

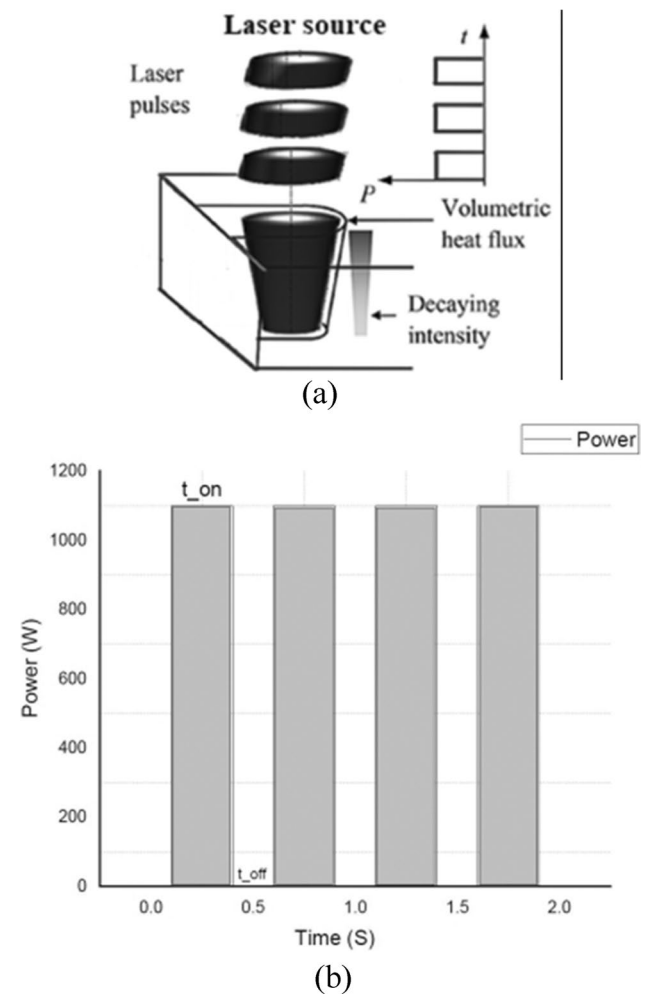
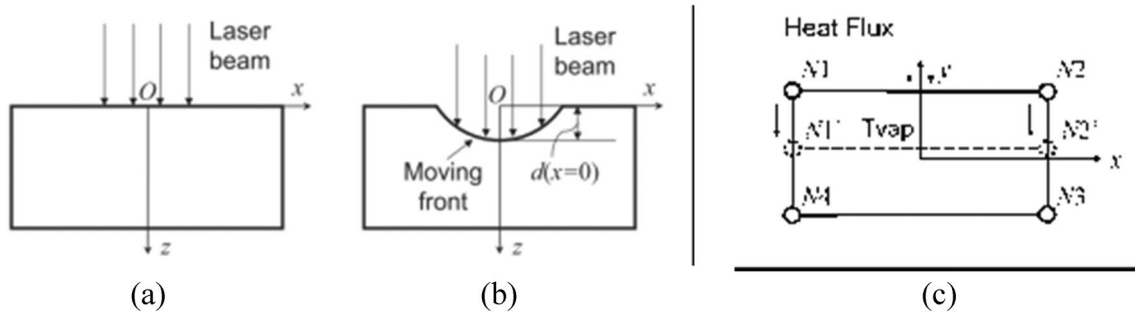


Fig. 5 a Schematic of pulse laser irradiation; b definition of laser pulses (MATLAB software)

uate the depth of material removal, so these two subroutines must be used simultaneously. In this study, a 2D axisymmetric FEM-based model is employed due to the circularity of the

Table 5 Required laser parameters for simulation

Parameters	d (mm)	M^2	f (Hz)	f_c (mm)	λ (nm)	P_{peak} (W)	A_s	R (mm)
Values	30	1.05	250-500-750	50	1080	500-600-700	0.8	0.5

**Fig. 6** Schematic of modelling material removal **a** beginning of laser beam strikes **b** During laser ablation **c** Calculation method based on Node temperature

cross sections and the laser beam, allowing us to estimate the geometrical features and temperature distribution for validation with experimental results. Firstly, some critical assumptions forming the basis of this research are listed. Then, the governing equations, boundary conditions, heat source model, programming of the pulsed laser, temperature-dependent properties, mesh moving algorithm, and meshing are briefly explained. The governing equation used is for determining the transient heat transfer within the axisymmetric sheet.

The FEA incorporates the UMESHMOTION subroutine and the ALE adaptive remesh algorithm to obtain the temperature solution for calculating the instant ablation rate at each time increment (Fig. 3). The surface nodes of the material move to new positions based on the ablation rate, resulting in a reduction in volume and mass of the material. Additionally, the entire computational domain is remeshed using the ALE adaptive remesh algorithm after the movement of surface nodes. The new mesh is then used to solve the laser heat conduction for the next time increment, ensuring a tight connection between surface recession and heat conduction. It is important to note that the ablated material is completely removed from the simulation domain, and the reduction in internal energy due to material removal is automatically considered in the numerical procedure.

4.1 Assumptions

In LBPMD modeling, several challenges are involved, including phase transformation, high-temperature gradients, and plasma formation. To accurately simulate this process,

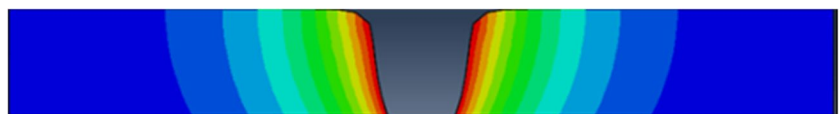
the model being used must adequately capture the actual characteristics of the process. In order to ensure a proper simulation, the following hypotheses have been taken into consideration [28]:

1. The proposed material is isotropic and homogeneous with temperature-dependent properties.
2. The input laser heat flux is considered a Gaussian beam distribution and is defined as a surface heat flux.
3. The plasma formation, melt flow, and recoil pressure inside the hole were ignored.
4. The laser beam is absorbed on the surface and transferred vertically downward.
5. The heat transfer within the molten pool was ignored.
6. The molten material is considered transparent and does not absorb the laser energy.
7. The vaporization stage results in removal of material in laser drilling. So in this research, element deletion is taken into account.

4.2 Governing equations

When laser energy is absorbed, it leads to a rapid increase in temperature on the surface of the solid material. With the incorporation of convective and radiative heat exchanges, the thermal behavior of the solid material is governed by the provided energy balance equation in Eq. 4:

$$\rho(T)C_p(T)(\partial T/\partial t - S^- \partial T/\partial z) - \nabla \cdot (k\nabla T) = q^- \quad (4)$$

Fig. 7 Drilled hole with the mesh moving procedure

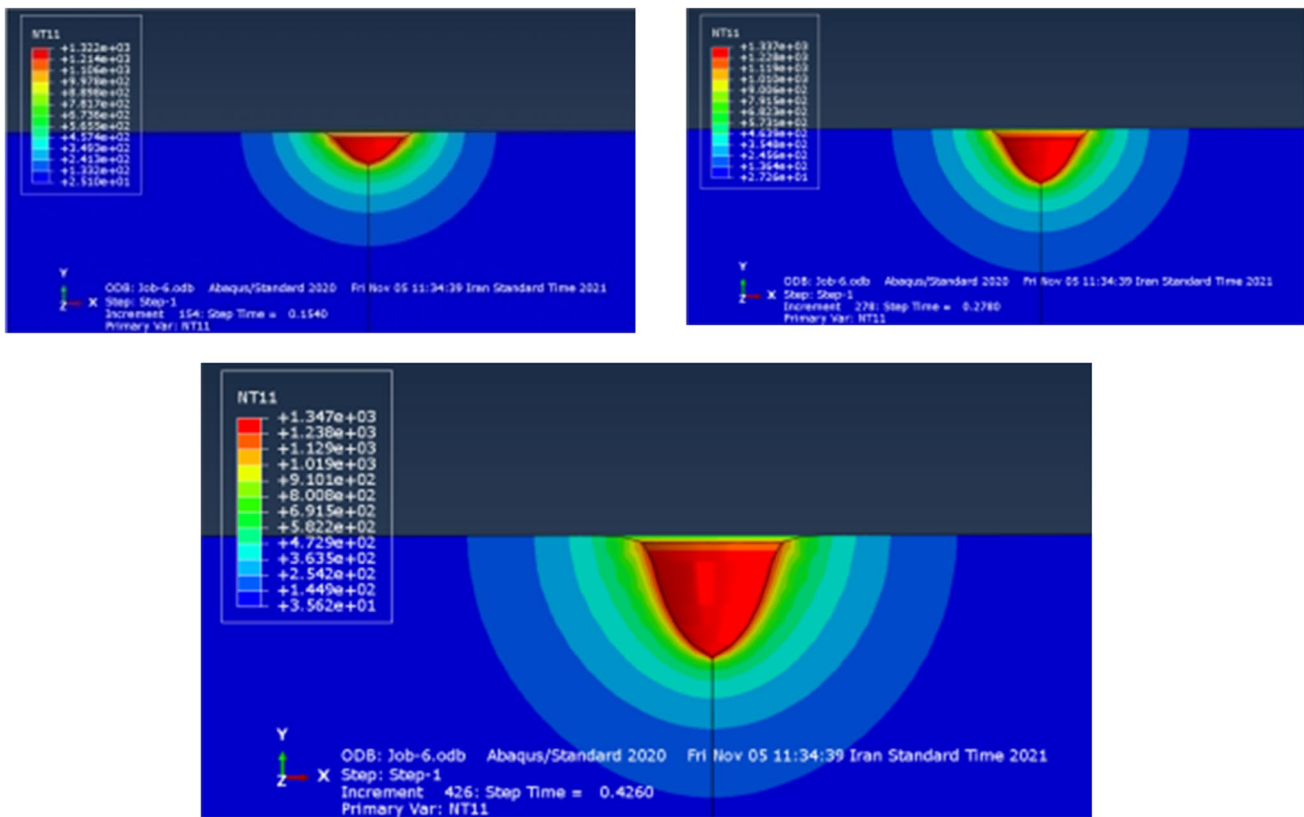


Fig. 8 Laser drilling simulation in different stages

where T is the temperature, $\rho(T)$ is the temperature-dependent density, $C(T)$ represents the temperature-dependent specific heat, $k(T)$ is the temperature-dependent thermal conductivity, S^* is the material removal rate (i.e., material removal), and q^* is the rate of energy density input from the laser source. The used materials in this research are considered homogeneous.

4.3 Boundary conditions

Figure 4 illustrates an axisymmetric model with accurate boundary conditions that yield ideal results for modeling the LBPM process. In this study, the laser beam is treated as a Gaussian-distributed heat source with an M^2 value of 1.05. The boundary conditions associated with Eq. 4 are divided into several sections. In the first step, the initial temperature of the model is assumed to be equal to the ambient temperature. The governing thermal boundary conditions of the model are presented in Eqs. 5–7 [29]. Here, τ represents the pulse width, and $T = 1/f$ denotes the total period of each pulse.

When $0 < t < \tau$:

$$k_{(T)} \frac{\partial(r, z, t)}{\partial z} = \begin{cases} h_{(T(r,z,t))} - T_0 & \text{for } r > R \text{ on } B_1 \\ q_{in} & \text{for } r \leq R \text{ on } B_1 \end{cases} \quad (5)$$

Whenever $\tau < t < T$:

$$k_{(T)} \frac{\partial(r, z, t)}{\partial z} = h_{(T(r,z,t)-T_0)} \text{ on } B_1 \quad (6)$$

Whenever $t > 0$:

$$k_{(T)} \frac{\partial(r, z, t)}{\partial z} = 0 \text{ on } B_2, B_3, \text{ and } B_4 \quad (7)$$

In the LBPM process, the surface of the target material is exposed to extreme temperature changes. Therefore,

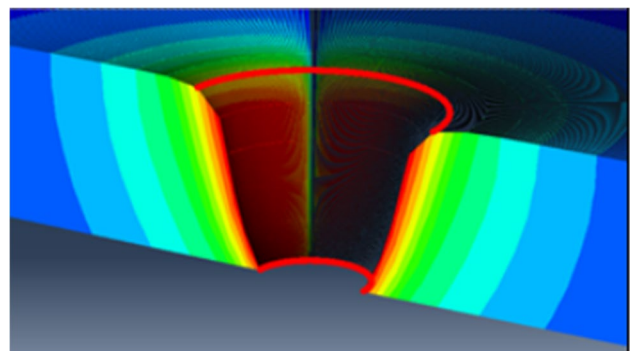


Fig. 9 Inlet and outlet hole diameter measurement

Table 6 Comparison between predicted and measured results

No.	Input variables				Errors	
	Laser power (W)	Laser pulse frequency (Hz)	Duty cycle (%)	Focal plane position (mm)	Inlet diameter (%)	Outlet diameter (%)
1	500	1000	40	8	11.62326	4.72
2	700	1000	40	8	6.5	27.53333
3	500	20,000	40	8	2.4675	22.91667
4	700	20,000	40	8	9.166667	7.333333
5	500	1000	60	8	1.593023	3.575758
6	700	1000	60	8	5.943396	1.268293
7	500	20,000	60	8	0	0
8	700	20,000	60	8	14.94	9.125
9	500	1000	40	12	11.26909	0.171429
10	700	1000	40	12	9.35625	4.626667
11	500	20,000	40	12	14.61538	0
12	700	20,000	40	12	0.883333	33.43919
13	500	1000	60	12	3.805556	4.652778
14	700	1000	60	12	16.06349	14.44156
15	500	20,000	60	12	0	0
16	700	20,000	60	12	5.335	3.322368
17	500	10,000	50	10	4.427083	4.928571
18	700	10,000	50	10	1.08	23.66667
19	600	1000	50	10	2.381818	29.7
20	600	20,000	50	10	14.67925	37.15094
21	600	10,000	40	10	4.245283	15.13636
22	600	10,000	60	10	14.69231	16.23333
23	600	10,000	50	8	3.854167	24.56863
24	600	10,000	50	12	3.333333	0
25	600	10,000	50	10	11.0283	15.44262
26	600	10,000	50	10	15.32075	14.7541

significant heat transfer occurs through radiation, which should be considered a highly important heat loss factor in this process. The Stefan-Boltzmann law describes the radiation heat loss from the workpiece's surface:

$$q_{\text{rad}} = \sigma \varepsilon (T_s^4 - T_\infty^4) \quad (8)$$

In Eq. 8, T_s and T_∞ are the surface temperature of the workpiece and the ambient temperature of the environment respectively. ε is the emissivity coefficient of radiation, which is 0.9 [18]. σ is the value of the Boltzmann constant, which equals 5.67×10^8 . The ambient temperature is considered 298 K.

To consider the heat losses as the result of the assisted gas, the convection heat coefficient was assumed to be 200 W/m² K [18]. The Newton cooling law expresses the convection heat loss from the workpiece's surface as Eq. 9. h is the convection heat coefficient, and A shows the area of the target material.

$$q = Ah(T_s - T_\infty) \quad (9)$$

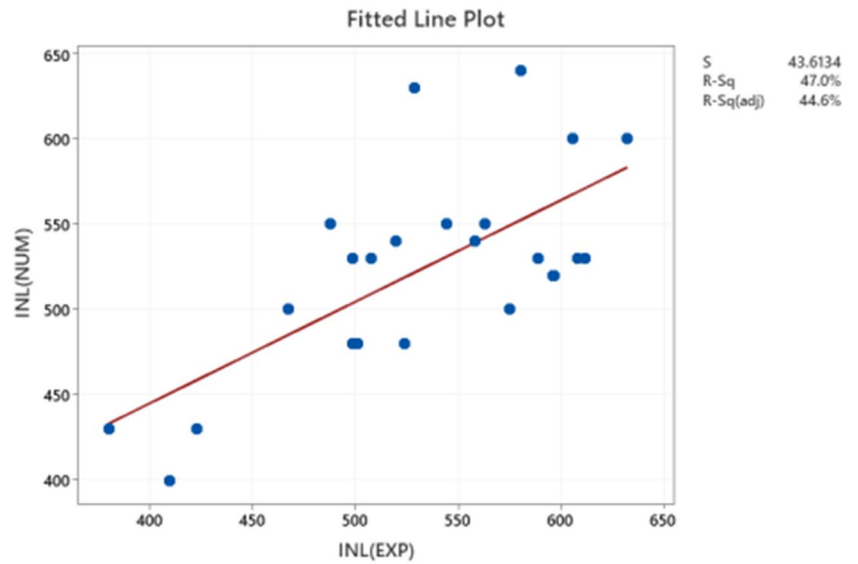
4.4 Temperature-dependent thermo-physical properties

Once the laser beam irradiates the surface of the sheet and transfers heat inside, the temperature increases rapidly due to interactions within the material. Since laser drilling involves melting and evaporation of the material, it is necessary to consider temperature-dependent properties when simulating the removal of material during the process. In this study, the temperature-dependent properties of Hastelloy X, as shown in Table 3, are used based on literature sources [30].

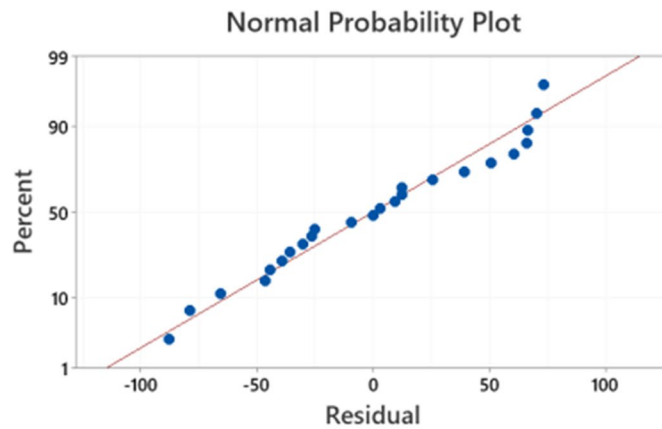
4.5 Appropriate heat source model

To model the laser heat source for the drilling process, it is highly recommended to use a radially symmetric disk with a Gaussian distribution. This disk represents the surface heat flux. Additionally, the body heat flux is defined by considering the change of the laser beam

Fig. 10 **a** Plot of experimental vs. predicted values for inlet diameter in a regression model. **b** Normal probability plot for the regression model of inlet diameter



(a)



(b)

radius with the depth of the target material. In Eq. 10, A_s represents the absorptivity, $P(f,m,t)$ is the laser power function, and P_{peak} is the peak power. According to Eq. 11, R is the laser effective beam radius, which is a function of the hole depth caused by defocusing. The variable r represents the radial distance from the laser axis, λ is the laser wavelength, z_m is the melt depth, d is the laser beam diameter, f_c is the laser focal length from the lens, and f is the laser frequency (repetition rate). It is important to note that in the DFLUX subroutine, as the mesh moves via the UMESHMOTION subroutine to form a drilled hole, z_m must be adjusted to the surface of the workpiece ($z_m = z - d$). The value of d (in mm) represents the removed depth due to reaching the vaporization temperature [29].

$$Q_{in} = (2A_s P(f, m, t)) / (\pi R^2) \exp(-2r^2/R^2) \tag{10}$$

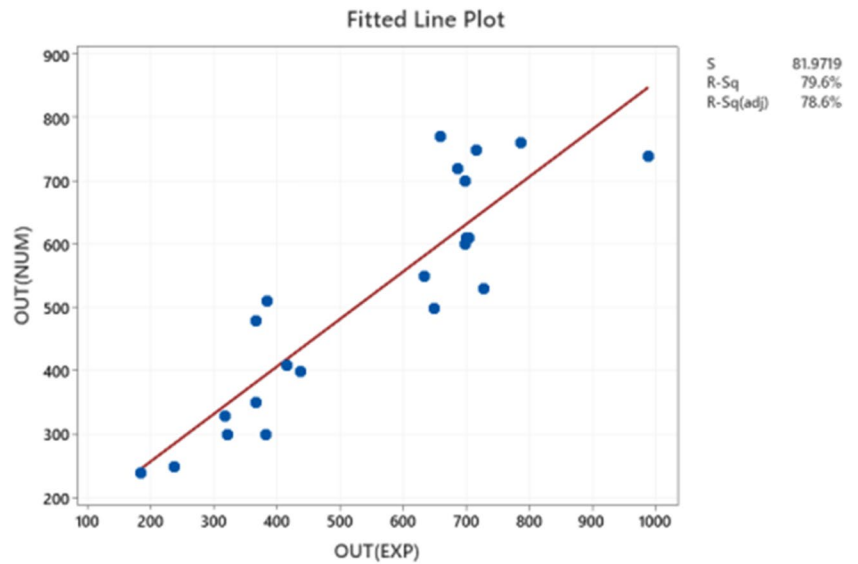
$$R = d/2 \left[1 + \left(4 \frac{M^2 \lambda (z_m + f_c)}{\pi d^2} \right) \right] \tag{11}$$

For a more detailed investigation, absorptivity is defined as a function of the irradiated laser beam’s wavelength and the temperature of the sheet according to Eq. 12 [31]. It should be noted that the absorptivity is higher for shorter laser beam wavelengths and increases with the rise in material temperature.

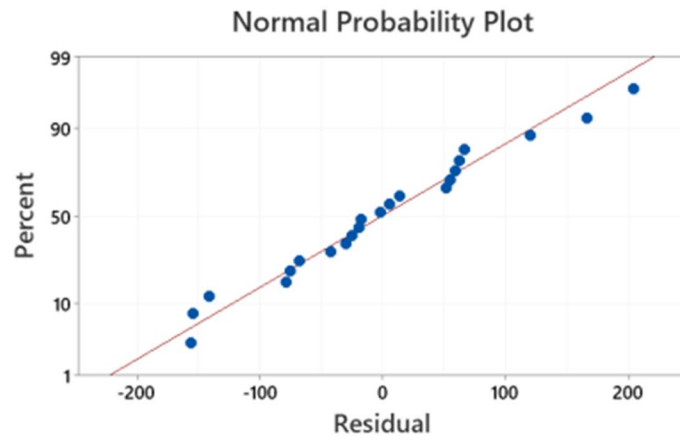
$$A_s = \sqrt{\frac{4\pi c \epsilon_0 [1 + \alpha_r (T(r, t) - T_0(r, t))]}{\lambda \sigma_0}} \tag{12}$$

where ϵ_0 shows the permittivity of vacuum, α_r is the coefficient of resistance of the sheet, λ is the wavelength of the fiber laser beam, c (1/ms) is the light velocity, and σ_0 is the target conductance at the initial temperature. Table 4 shows the values of the above parameters for Hastelloy X [30].

Fig. 11 **a** Plot of experimental vs. predicted values for outlet diameter in a regression model. **b** Normal probability plot for the regression model of outlet diameter



(a)



(b)

Table 7 Regression model summary for inlet hole diameter

<i>S</i>	<i>R</i> -sq	<i>R</i> -sq(adj)
50.2043	47.03%	44.62%

Table 8 Regression model summary for outlet hole diameter

<i>S</i>	<i>R</i> -sq	<i>R</i> -sq(adj)
97.4872	79.61%	78.59%

4.6 Implementation of pulsed (percussion) laser heat source

In order to gain a theoretical understanding of the laser percussion micro-drilling process, a schematic of the pulsed 3D heat flux and the definition of laser pulse parameters are shown in Fig. 5. To simulate the

characteristics of the heat flux generated by laser pulses, a DFLUX user subroutine for the mentioned heat source model was developed [32].

The first step in simulating percussion laser drilling is to consider pulse operation. Therefore, it is necessary to define the modulated laser power as a function of laser frequency f . The period is defined as T , while t_{off} and t_{on} represent the pulse interval and pulse width time, respectively, as shown in Eq. 14. In this research, the laser pulse shape is defined as a perfectly rectangular pulse with a sine function, according to Eq. 16. During the pulse duration time, the laser power P is equal to P_{peak} . However, P is equal to zero when there is no pulse within one period.

$$\omega = 2 \times \pi \times f \tag{13}$$

$$t_{off} = (T - t_{on}) \tag{14}$$

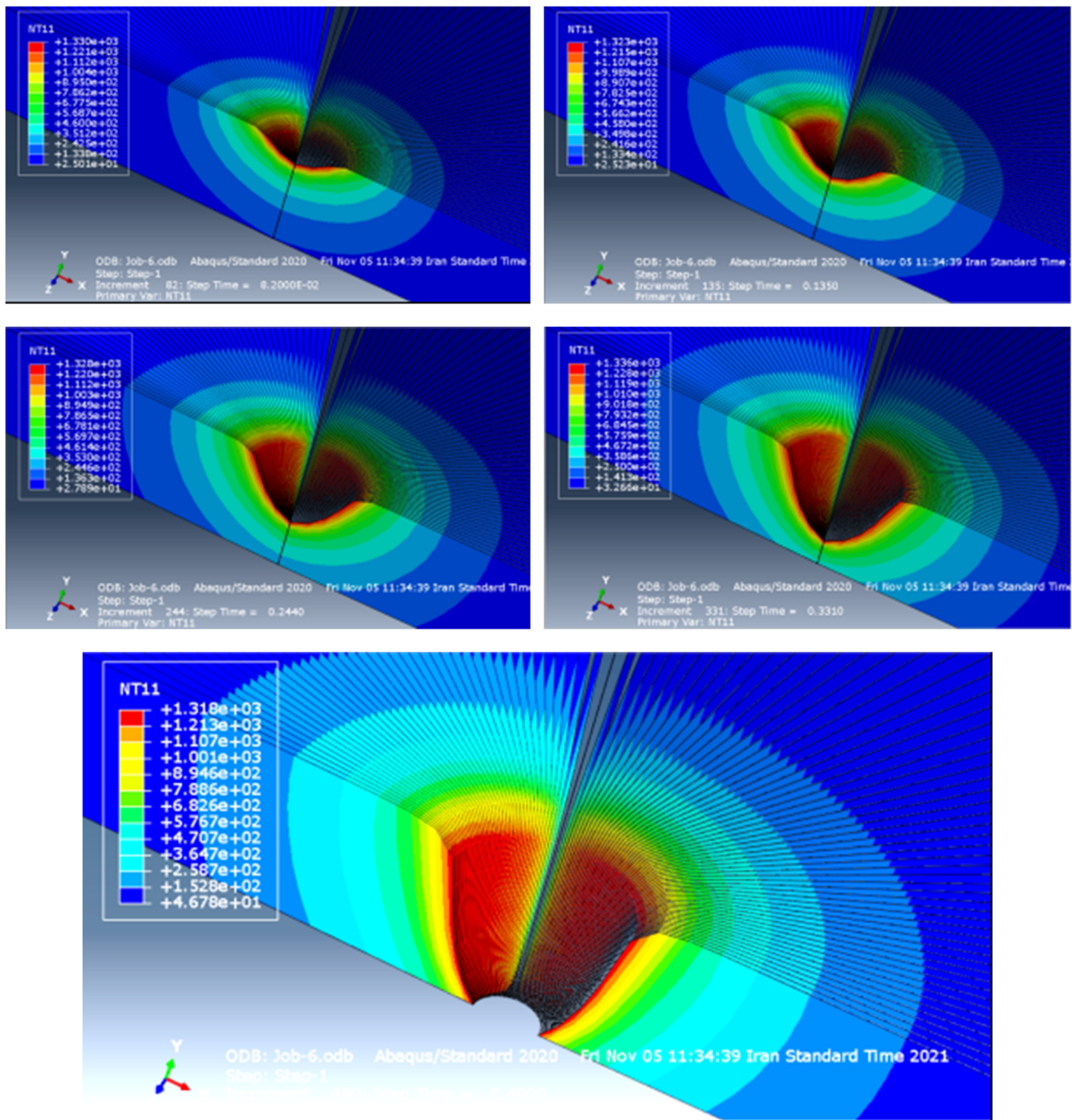


Fig. 12 Five steps of simulation laser drilling case (17)

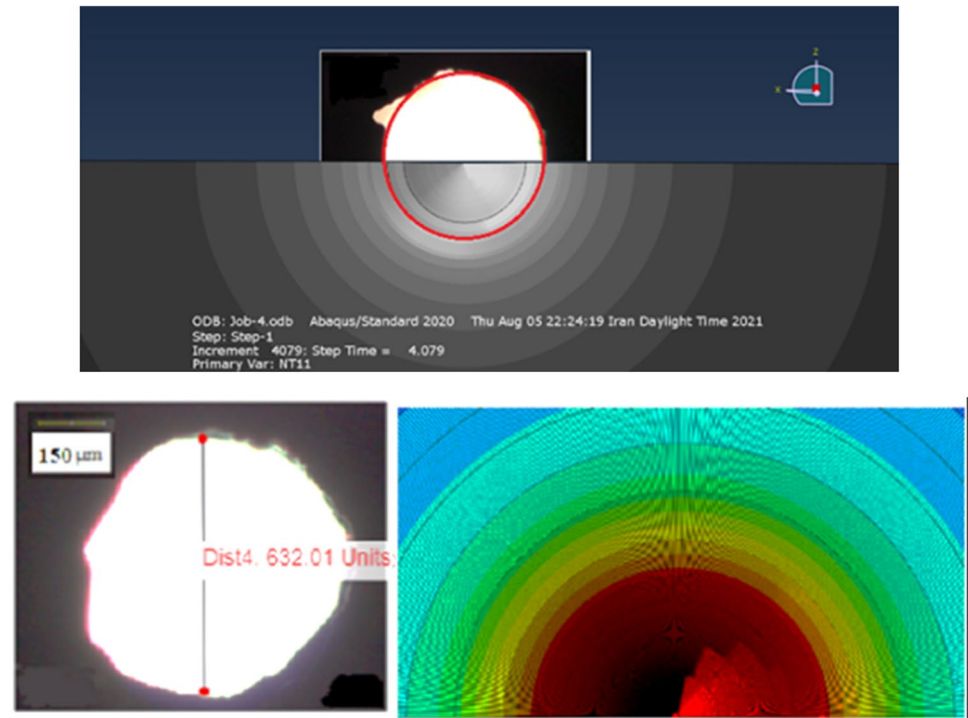
$$A = \frac{1}{\sin(\omega \times t_{off})} \tag{15}$$

$$P = P_{peak} \times \text{Int}(A \times \text{abs}(\sin(\omega \times T))) \tag{16}$$

Besides, the P_{peak} value as the maximum instantaneous optical power output by the laser can be obtained using Eq. 17:

$$P_{peak}(W) = \frac{P_{avg}(W) \times 1000}{f(Hz) \times \text{pulse width}(ms)} \tag{17}$$

Fig. 13 Comparison between experimental and simulation results



The novelty of modeling percussion laser drilling lies in simulating the stationary pulsed laser heat source, which provides more accurate spatial thermal loading. Additionally, all the process parameters that need to be determined on the laser machine are defined in this model and depicted in Table 5.

4.7 Novel element deletion method with mesh moving and adaptive remeshing algorithm in Abaqus

In this study, finite element analysis of the nonlinear heat transfer for laser percussion drilling is conducted using Abaqus. According to the literature, several techniques have been implemented in FEA software to model laser drilling. One of the most well-known methods is the element deletion technique, which deletes elements once their temperature reaches a specific value. However, despite the advantages and simplifications of this method, the heat flux boundary cannot be properly updated after elements are deleted. In contrast, the current novel method offers an alternative approach with the UMESHMOTION subroutine, which allows the user to define mesh movement corresponding to various field variables, such as temperature. Therefore, in this technique, when the surface temperature reaches a specific temperature (vaporization temperature), an evaporation phenomenon takes place, and the material is instantly removed after each time increment. Additionally, the ALE mesh algorithm regenerates the mesh after the downward movement of

surface nodes parallel to their direction. It should be noted that the boundary conditions, including convection and radiation, can also be automatically updated. Furthermore, the ALE mesh algorithm minimizes mesh distortions and helps to improve the smoothness of the simulation. The schematic of the numerical procedure is shown in Fig. 6 [27]. Fig. 6 c demonstrates the procedure to calculate the temperature of each node and material removal, respectively. The contour result of the LBPMD process is shown in Fig. 7.

It is assumed that evaporation occurs when a portion of the element area surpasses the vaporization temperature T_{vap} . Consequently, the surface nodes move to their new positions based on the instantaneous material removal rate. As a result, both the volume and mass of the workpiece are reduced accordingly. The motion of the nodes is programmed by moving the upper nodes N_1 and N_2 , whose temperature exceeds the vaporization temperature of the workpiece to the exact receding surface, where the temperature is set to $T = T_{\text{vap}}$ (if $T_{N1} > T_{\text{vap}}$, $T_{N4} < T_{\text{vap}}$ is satisfied). Figure 8 illustrates the different phases of hole formation during the LBPMD process with the proposed model.

4.8 Mesh

The material's computational domain represents the right half of the workpiece and has dimensions of 5 mm in length and 2 mm in thickness. To ensure accuracy, a fine mesh is applied specifically to the heated surface, with a fine element size of $50 \mu\text{m} \times 50 \mu\text{m}$. In other areas, a

Table 9 Experimental result overview

No.	Input variables					Experimental output parameters						
	Laser power (W)	Laser pulse frequency (Hz)	Duty cycle (%)	Focal plane position (mm)	Time of drilling	Pulse width (μs)	Laser intensity (MW/cm ²)	Inlet diameter (μm)	Outlet diameter (μm)	Hole taper angle (°)	Inlet circularity	
1	500	1000	40	8	1.15	400	24.9	380.02	238.2	4.270	0.805	
2	700	1000	40	8	0.44	400	34.8	467.5	382.6	2.430	0.735	
3	500	20,000	40	8	0.51	20	24.9	409.87	185	6.250	0.904	
4	700	20,000	40	8	0.4	20	34.8	524	322	5.770	0.835	
5	500	1000	60	8	0.85	600	16.6	423.15	318.2	3.005	0.7	
6	700	1000	60	8	0.35	600	23.2	498.5	415.2	2.100	0.625	
7	500	20,000	60	8	-	30	16.6	No hole	-	-	-	
8	700	20,000	60	8	0.3	30	23.2	574.7	436.5	3.950	0.695	
9	500	1000	40	12	1.5	400	24.9	488.02	698.8	5.980	0.763	
10	700	1000	40	12	0.65	400	34.8	580.12	715.3	3.910	0.684	
11	500	20,000	40	12	0.64	20	24.9	596	blind	-	-	
12	700	20,000	40	12	0.47	20	34.8	605.3	987.45	10.820	0.8	
13	500	1000	60	12	1	600	16.6	519.45	686.5	4.770	0.658	
14	700	1000	60	12	0.52	600	23.2	528.8	658.8	3.710	0.584	
15	500	20,000	60	12	0.6	30	16.6	No hole	-	-	-	
16	700	20,000	60	12	0.38	30	23.2	632.01	785.25	4.570	0.645	
17	500	10,000	50	10	1.5	50	19.9	501.25	367.25	3.830	0.768	
18	700	10,000	50	10	0.4	50	27.9	544.06	366.4	5.100	0.712	
19	600	1000	50	10	1	500	23.9	563.1	648.5	2.440	0.689	
20	600	20,000	50	10	0.4	25	23.9	607.8	726.9	3.400	0.83	
21	600	10,000	40	10	0.55	40	29.8	507.5	633.25	3.640	0.802	
22	600	10,000	60	10	0.5	60	19.9	596.4	697.4	2.890	0.65	
23	600	10,000	50	8	0.45	50	23.9	498.5	384.7	3.250	0.723	
24	600	10,000	50	12	0.6	50	23.9	558	Blind	-	-	
25	600	10,000	50	10	0.55	50	23.9	588.45	704.2	3.310	0.785	
26	600	10,000	50	10	0.5	50	23.9	611.2	700	2.540	0.765	

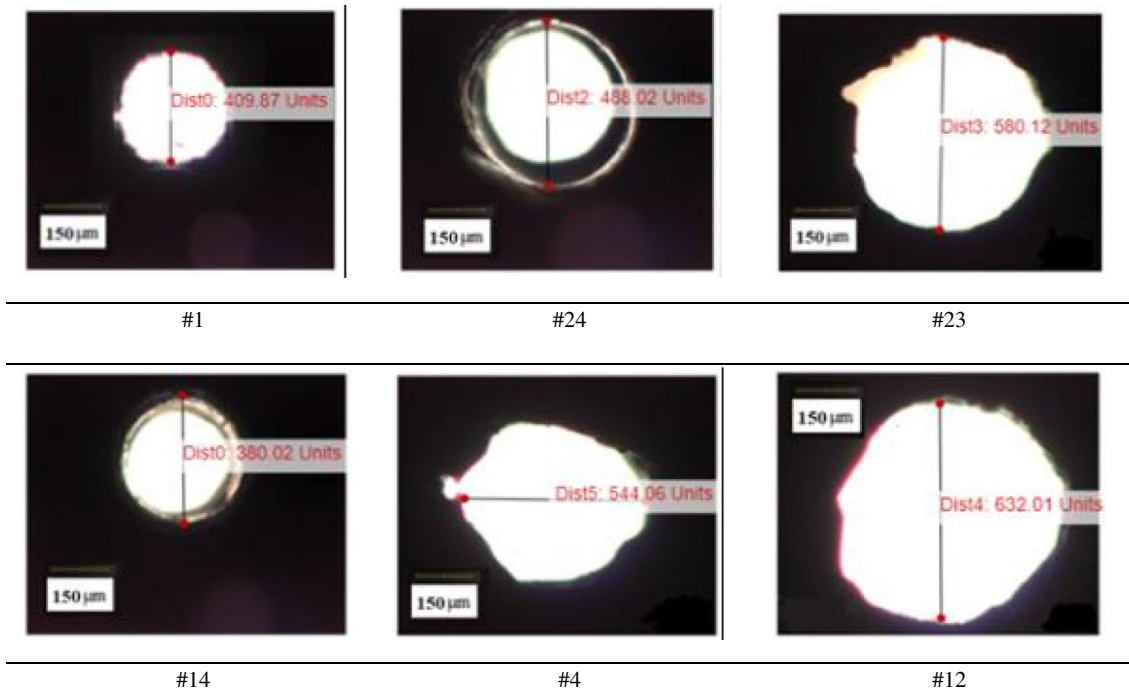


Fig. 14 Selected drilled holes’ dimensions

Table 10 Unrevised ANOVA of the inlet hole diameter

Source	DF	Adj SS	Adj MS	F-value	P-value
Model	14	94,987	6784.8	8.36	0.002
Linear	4	70,137	17,534.2	21.61	0.000
<i>P</i> (W)	1	7103	7103.2	8.75	0.016
<i>f</i> (Hz)	1	13,743	13,742.8	16.94	0.003
<i>D</i> (%)	1	4512	4512.3	5.56	0.043
<i>FPP</i> (mm)	1	31,305	31,305.4	38.58	0.000
Square	4	11,925	2981.2	3.67	0.049
<i>P</i> (W) × <i>P</i> (W)	1	3217	3216.6	3.96	0.078
<i>f</i> (Hz) × <i>f</i> (Hz)	1	1562	1562.4	1.93	0.199
<i>D</i> (%) × <i>D</i> (%)	1	118	117.6	0.14	0.712
<i>FPP</i> (mm) × <i>FPP</i> (mm)	1	2358	2358.0	2.91	0.122
2-way interaction	6	7704	1284.0	1.58	0.257
<i>P</i> (W) × <i>f</i> (Hz)	1	266	266.4	0.33	0.581
<i>P</i> (W) × <i>D</i> (%)	1	1102	1102.1	1.36	0.274
<i>P</i> (W) × <i>FPP</i> (mm)	1	2491	2490.5	3.07	0.114
<i>f</i> (Hz) × <i>D</i> (%)	1	1188	1187.6	1.46	0.257
<i>f</i> (Hz) × <i>FPP</i> (mm)	1	427	426.5	0.53	0.487
<i>D</i> (%) × <i>FPP</i> (mm)	1	2061	2060.8	2.54	0.145
Error	9	7302	811.4		
Lack of fit	8	7044	880.5	3.40	0.398
Pure error	1	259	258.8		
Total	23	102,289			

Table 11 Revised ANOVA of the inlet hole diameter

Source	DF	Adj SS	Adj MS	F-value	P-value
Model	4	71,699	17,924.7	10.85	0.000
Linear	4	71,699	17,924.7	10.85	0.000
<i>P</i>	1	11,670	11,670.0	7.07	0.016
<i>f</i>	1	16,779	16,779.3	10.16	0.005
<i>D</i>	1	4574	4573.6	2.77	0.113
<i>FPP</i>	1	33,515	33,514.6	20.29	0.000
Error	19	31,383	1651.7		
Lack of fit	18	31,124	1729.1	6.68	0.297
Pure error	1	259	258.8		
Total	23	103,081			

coarser mesh is used. Extensive mesh refinement studies have been conducted, confirming that the mesh size employed in the current simulation is sufficiently accurate. The modeling domain utilizes the CAX4T element type, which consists of four-node bilinear displacement

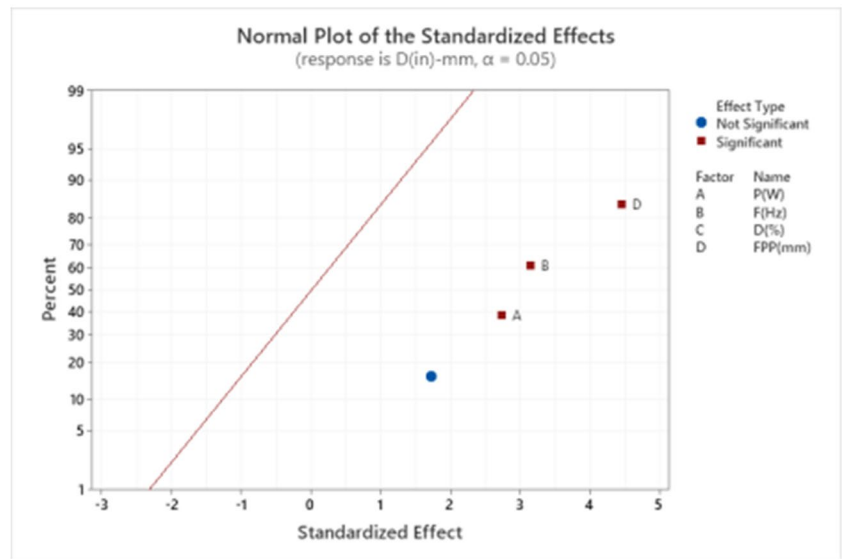
Table 12 Model adequacy for the inlet diameter

S	R-sq	R-sq(adj)	R-sq(pred)
0.0256492	96.48%	89.44%	68.64%

Fig. 15 **a** Normal plot before modifying the model. **b** Normal plot for the modified model



(a)



(b)

and temperature elements. The computations are carried out on a laptop equipped with a dual-core processor and 32 GB of RAM. Given the high-temperature changes in these thermal simulations, it is necessary to use smaller time increments to ensure compliance with the maximum allowable temperature change per increment.

4.9 Validation

The developed FEA model was validated using experimental data for the inlet and outlet diameters. A total of 26 different cases, designed based on the RSM, were compared using the obtained results. The Visilog software was utilized to precisely measure the inlet and outlet diameters of each drilled

hole in the experimental outputs. In the simulation with Abaqus, we focused solely on the inlet and outlet diameters as the response variables. Figure 9 presents the numerical results for the inlet and outlet diameters of the laser-drilled hole. The average relative error between the experimental and predicted values using the model was found to be 7.25% for the inlet diameter and 12.258% for the outlet diameter. These errors fall within acceptable ranges. A detailed comparison between the simulated and experimental results is provided in Table 6.

In Figs. 10a and 11a, inlet and outlet diameters are compared between measured results and predicted ones in the regression model, respectively. In Figs. 10b and 11b, the normal probability of the regression model for inlet and outlet diameters are demonstrated. The regression equations for

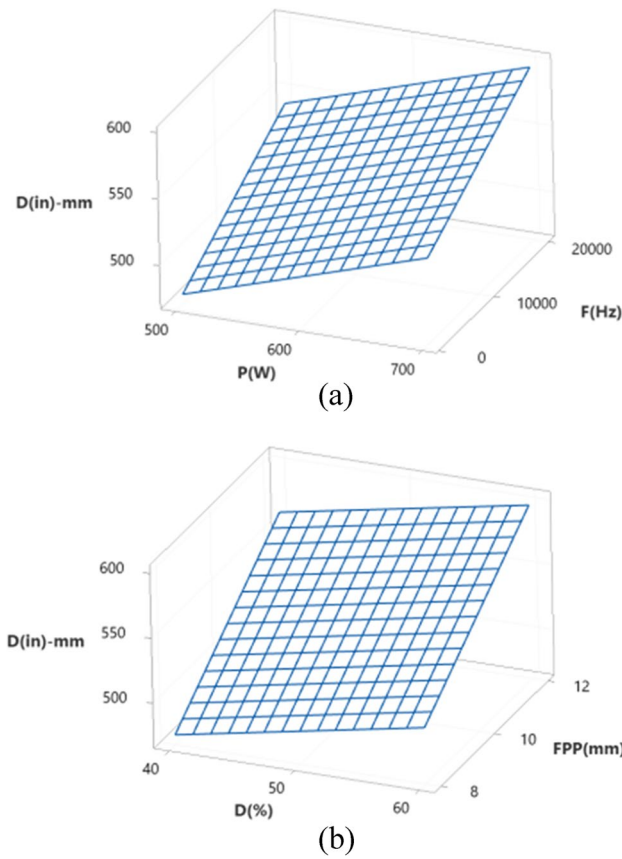


Fig. 16 Surface plots for inlet diameter: **a** laser power versus laser frequency; **b** duty cycle versus focal plane position

$D(\text{in})_{\text{EXP}}$ and $D(\text{Out})_{\text{EXP}}$ are presented as Eqs. 18 and 19, respectively. The ANOVA in Tables 7 and 8 confirms that the regression model provides a good estimation for the fitted interpolation lines. The obtained regression equation is considered significant, while the lack of fit is deemed insignificant. Figure 12 accurately illustrates the five stages of hole formation at different time increments for the no. 17 case. Additionally, Fig. 13 showcases the comparison of diameter measurements between the numerical and experimental outputs.

$$D(\text{in})_{\text{EXP}} = 119.4 + 0.7894 \times D(\text{in})_{\text{NUM}} \tag{18}$$

$$D(\text{Out})_{\text{EXP}} = 2.23 + 1.061 \times D(\text{Out})_{\text{NUM}} \tag{19}$$

5 Statistical modeling

In this study, the response surface methodology was used for the DOE with the assistance of the Minitab 2019 software. Each of the input parameters, including laser power

Table 13 Unrevised ANOVA of hole taper angle

Source	DF	Adj SS	Adj MS	F-value	P-value
Model	14	67.6633	4.8331	4.85	0.022
Linear	4	33.8280	8.4570	8.49	0.008
P (W)	1	0.0180	0.0180	0.02	0.897
f (Hz)	1	5.7583	5.7583	5.78	0.047
D (%)	1	15.9787	15.9787	16.03	0.005
FPP (mm)	1	8.8245	8.8245	8.86	0.021
Square	4	8.6255	2.1564	2.16	0.175
P (W) \times P (W)	1	2.8953	2.8953	2.91	0.132
f (Hz) \times f (Hz)	1	0.4729	0.4729	0.47	0.513
D (%) \times D (%)	1	0.0101	0.0101	0.01	0.923
FPP (mm) \times FPP (mm)	1	0.9602	0.9602	0.96	0.359
2-way interaction	6	12.2539	2.0423	2.05	0.185
P (W) \times f (Hz)	1	3.1042	3.1042	3.11	0.121
P (W) \times D (%)	1	0.5922	0.5922	0.59	0.466
P (W) \times FPP (mm)	1	0.0464	0.0464	0.05	0.835
f (Hz) \times D (%)	1	8.2474	8.2474	8.28	0.024
f (Hz) \times FPP (mm)	1	0.3506	0.3506	0.35	0.572
D (%) \times FPP (mm)	1	1.2231	1.2231	1.23	0.305
Error	7	6.9758	0.9965		
Lack of fit	6	6.6794	1.1132	3.76	0.376
Pure error	1	0.2964	0.2964		
Total	21	74.6391			

(P), duty cycle % (D), focal plane position (FPP), and laser frequency (f), was assigned three levels, resulting in a total of 26 experiments. The responses analyzed in this study were the inlet diameter, outlet diameter, hole taper angle, and inlet circularity, and their summarized results can be found in Table 9. ANOVA was employed to determine the mathematical models for the responses, and subsequently, the input factors were optimized using Minitab 2019. The significant factors and the highest

Table 14 Revised ANOVA of hole taper angle

Source	DF	Adj SS	Adj MS	F-value	P-value
Model	4	46.4075	11.6019	6.99	0.002
Linear	3	42.5215	14.1738	8.53	0.001
f (Hz)	1	13.2671	13.2671	7.99	0.012
D (%)	1	16.4171	16.4171	9.89	0.006
FPP (mm)	1	13.9752	13.9752	8.42	0.010
2-way interaction	1	7.6638	7.6638	4.61	0.046
f (Hz) \times D (%)	1	7.6638	7.6638	4.61	0.046
Error	17	28.2316	1.6607		
Lack of fit	16	27.9351	1.7459	5.89	0.314
Pure error	1	0.2964	0.2964		
Total	21	74.6391			

Table 15 Model adequacy for hole taper angle

S	R-sq	R-sq(adj)	R-sq(pred)
1.28867	62.18%	53.28%	25.35%

polynomial order were identified based on criteria such as *P*-value and adjusted *R*². Figure 14 provides a visual representation of the drilled geometry and dimensions for some selected tests listed in Table 9.

6 Results and discussion

The responses analyzed in this study included the inlet hole diameter, outlet hole diameter, inlet circularity, and hole taper angle. It is important to note that circularity at the hole exit is not a major concern in LBPMD, as the ejection of removed material tends to make the hole exits more circular. Therefore, the assessment of inlet circularity alone is sufficient. The effects of various laser process factors on these geometrical features were evaluated. ANOVA was conducted on the experimental results to identify significant input factors and investigate their impacts on the outputs. This analysis utilized full quadratic polynomial functions and was carried out using the Minitab 2019 statistical software. By examining the measured responses presented in Table 9, statistical information regarding the inlet and outlet hole diameters, inlet circularity, and hole taper angle in relation to variations can be extracted and analyzed using Minitab. The relationship between the geometrical features and laser process parameters is described in detail. Finally, a multi-objective optimization of the LBPMD process was performed to achieve the most desirable responses.

6.1 Inlet hole diameter

The equivalent entrance diameter provided in the analysis represents the nominal hole diameter. Hence, for each inlet hole, all responses were examined and discussed. In Table 10, primary results before modifying the model are represented. The ANOVA results in Table 11 indicate that all input factors, including laser power, laser frequency, focal plane position, and duty cycle, have a significant impact. The ANOVA in Table 12 confirms that the regression model provides a good estimation for the inlet hole diameter. The obtained regression equation is considered significant, while the lack of fit is deemed insignificant. However, according to Fig. 15, none of the interactions or quadratic terms were found to be significant. The regression equation derived from the analysis is considered significant, while the lack of fit is deemed insignificant. Therefore, based on the analysis and modified model, the final regression equation in terms of uncoded parameters is presented as Eq. 20.

$$D_{(in)} = 14.1 + 0.284 \times P(W) + 0.00345 \times F(Hz) + 1.79 \times D(\%) + 22.57 \times FPP(mm) \tag{20}$$

Figure 16 depicts the surface plot showcasing the impact of significant input parameters on the entrance hole diameter. The plot clearly shows that the highest value of each parameter corresponds to the largest diameter of the entrance hole. Increasing the laser power results in an enlargement of the

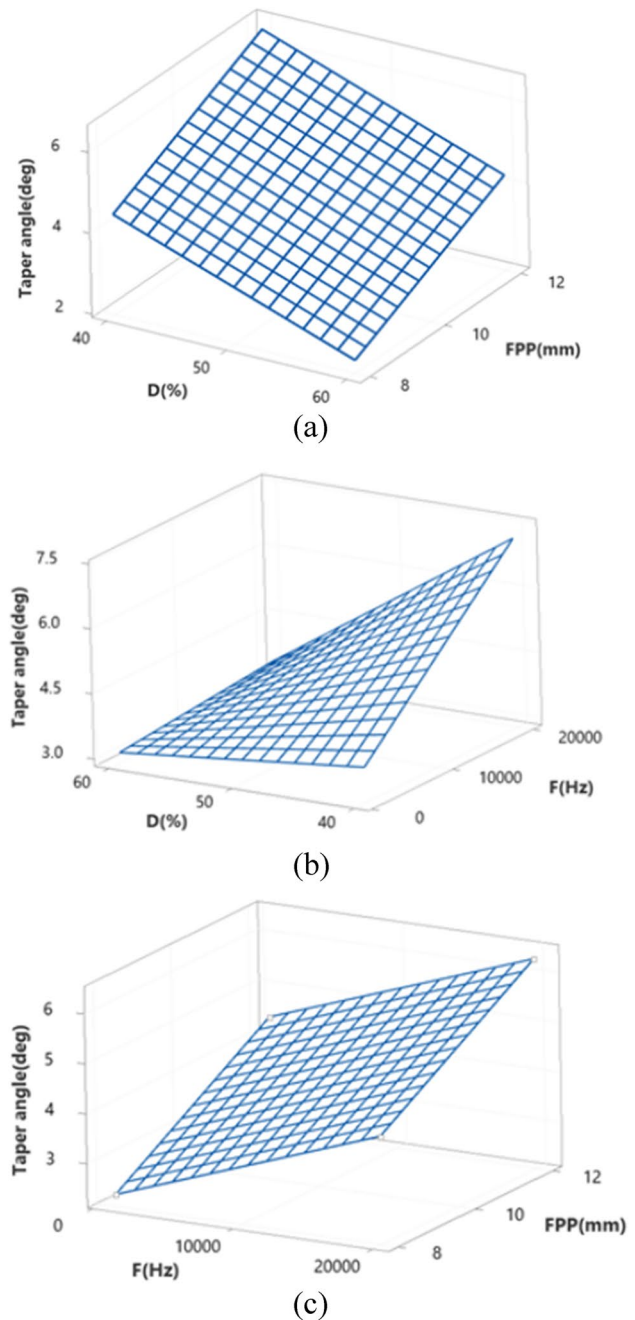


Fig. 17 Surface plots for hole taper angle: **a** duty cycle versus focal plane position; **b** duty cycle versus laser frequency; **c** laser frequency versus focal plane position

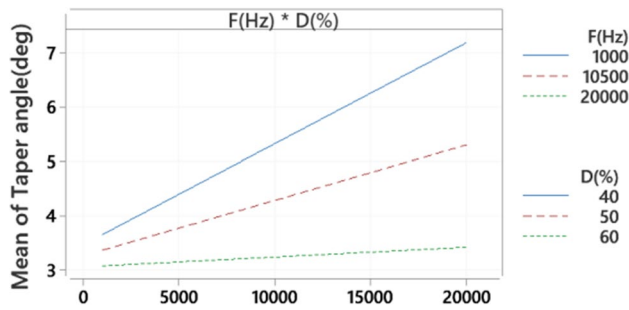


Fig. 18 Interaction plot for hole taper angle

entrance hole diameter. This happens since when adopting a higher laser power, the threshold energy is exceeded in a wider range of the Gaussian (i.e., part of the tails also is now able to vaporize the material). Similarly, a higher laser frequency leads to a larger entrance hole diameter, as indicated in Fig. 16. An increased laser frequency results in a greater accumulation of heat input irradiated onto the material. It is important to note that the laser frequency significantly affects the peak power of each pulse. Another notable observation is the combined effect when two adjacent pulses are irradiated on the target for a specific duration, causing the melt to solidify and resulting in the formation of hole blockages [33]. Therefore, based on this issue, a laser frequency higher than 20

Table 16 Unrevised ANOVA of inlet circularity

Source	DF	Adj SS	Adj MS	F-value	P-value
Model	14	0.126230	0.009016	13.71	0.001
Linear	4	0.112547	0.028137	42.77	0.000
<i>P</i> (W)	1	0.010006	0.010006	15.21	0.006
<i>f</i> (Hz)	1	0.016528	0.016528	25.12	0.002
<i>D</i> (%)	1	0.044614	0.044614	67.81	0.000
<i>FPP</i> (mm)	1	0.002804	0.002804	4.26	0.078
Square	4	0.002080	0.000520	0.79	0.567
<i>P</i> (W) × <i>P</i> (W)	1	0.000014	0.000014	0.02	0.889
<i>f</i> (Hz) × <i>f</i> (Hz)	1	0.000861	0.000861	1.31	0.290
<i>D</i> (%) × <i>D</i> (%)	1	0.000300	0.000300	0.46	0.521
<i>FPP</i> (mm) × <i>FPP</i> (mm)	1	0.000785	0.000785	1.19	0.311
2-way interaction	6	0.001388	0.000231	0.35	0.888
<i>P</i> (W) × <i>f</i> (Hz)	1	0.000000	0.000000	0.00	0.993
<i>P</i> (W) × <i>D</i> (%)	1	0.000002	0.000002	0.00	0.955
<i>P</i> (W) × <i>FPP</i> (mm)	1	0.000076	0.000076	0.12	0.744
<i>f</i> (Hz) × <i>D</i> (%)	1	0.001089	0.001089	1.66	0.239
<i>f</i> (Hz) × <i>FPP</i> (mm)	1	0.000067	0.000067	0.10	0.759
<i>D</i> (%) × <i>FPP</i> (mm)	1	0.000006	0.000006	0.01	0.927
Error	7	0.004605	0.000658		
Lack of fit	6	0.004405	0.000734	3.67	0.380
Pure error	1	0.000200	0.000200		
Total	21	0.130835			

Table 17 Revised ANOVA of inlet circularity

Source	DF	Adj SS	Adj MS	F-value	P-value
Model	3	0.117992	0.039331	55.12	0.000
Linear	3	0.117992	0.039331	55.12	0.000
<i>P</i> (W)	1	0.022323	0.022323	31.28	0.000
<i>f</i> (Hz)	1	0.034693	0.034693	48.62	0.000
<i>D</i> (%)	1	0.057197	0.057197	80.16	0.000
Error	18	0.012844	0.000714		
Lack of fit	17	0.012644	0.000744	3.72	0.389
Pure error	1	0.000200	0.000200		
Total	21	0.130835			

kHz was not chosen. As shown in Table 9, test no. 7 and no. 15 experienced a significant decline in laser pulse power (up to 30%), rendering the laser machine unable to drill the hole. The laser intensity decreased to 16.6 MW/cm² for these cases. Duty cycle, another input parameter, also influences the inlet hole diameter. Varying the duty cycle affects the pulse width, with an increase in duty cycle leading to a longer pulse width. This, in turn, extends the radiation time, allowing for a longer interaction between the target material and the laser beam and providing sufficient heat at the entrance hole. Finally, the focal plane position is examined. When the focal plane position is positive, the laser beam spot is located at the top of the target, resulting in a larger hole diameter on the surface.

6.2 Hole taper angle

In terms of hole taper, all the main effects of the parameters, except for laser power, have notable impacts. Table 13 indicates the unrevised ANOVA table. However, Table 14 provides evidence of the highly influential interaction between duty cycle (*D*) and laser frequency (*f*) among the second-order terms and interactions. The results demonstrate that laser frequency, duty cycle, and focal plane position have significant effects on the hole taper angle. Equation 21 presents the regression model in uncoded values for the hole taper angle, considering the significant parameters. The ANOVA in Table 15 confirms that the regression model provides a good estimation for the hole taper angle. The obtained regression equation is considered significant, while the lack of fit is deemed insignificant. When the regression model is deemed significant and the lack of fit is insignificant simultaneously, this indicates that the analysis has been carried out correctly.

$$\text{Taper angle } (^{\circ}) = -0.79 + 0.000521 \times f \text{ (Hz)} - 0.0204 \times D \text{ (\%)} + 0.507 \times FPP \text{ (mm)} - 0.000008 \times f \text{ (Hz)} \times D \text{ (\%)} \tag{21}$$

Table 18 Model adequacy for inlet circularity

S	R-sq	R-sq(adj)	R-sq(pred)
0.0267122	90.18%	88.55%	85.07%

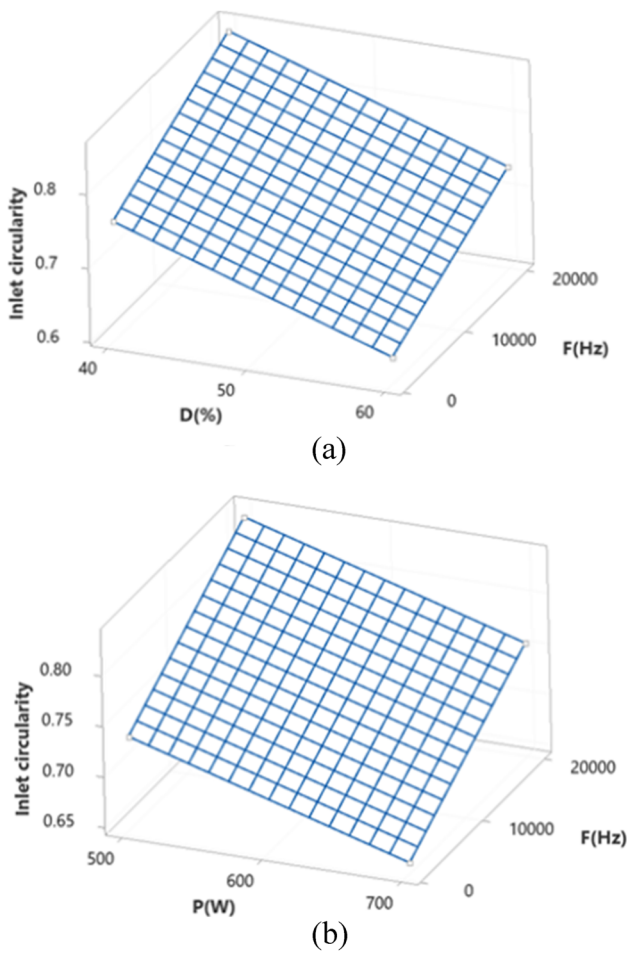


Fig. 19 Surface plots for inlet circularity. **a** Duty cycle versus laser frequency. **b** Laser power versus laser frequency

Figure 17a and c indicate that increasing the focal distance at a positive focal position significantly affects the exit hole due to the beam divergence effect. A higher focal plane position can lead to a larger outlet hole diameter, resulting in a higher hole taper angle. Additionally, Figs. 17b and 18 demonstrate that increasing the duty cycle and decreasing

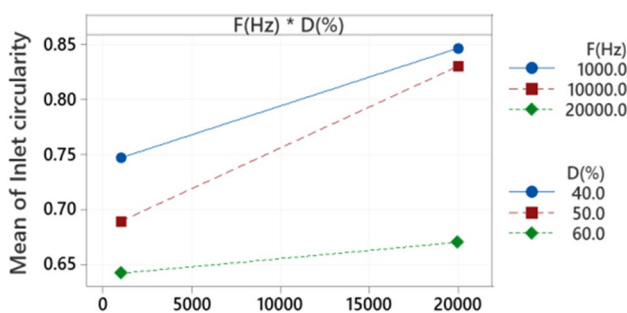


Fig. 20 Interaction plot for inlet circularity

Table 19 Comparison between statistical and simulation models for inlet hole diameter

Run	Error% statistical	Error% simulation
1	0.103136677	0.131519394
2	0.149463102	0.069518717
3	0.008524654	0.024080806
4	0.116076336	0.083969466
5	0.19370436	0.016188113
6	0.201636911	0.063189569
7	-	-
8	0.193433096	0.12998086
9	0.11662227	0.127002992
10	0.158956768	0.103220023
11	0.166684564	0.127516779
12	0.085650091	0.008755989
13	0.169383001	0.039561074
14	0.076656581	0.191376702
15	-	-
16	0.12372589	0.050647933
17	0.167690773	0.042394015
18	0.128781752	0.010917913
19	0.263816374	0.023264074
20	0.210110234	0.128002632
21	0.122333005	0.044334975
22	0.252558685	0.128101945
23	0.19668004	0.037111334
24	0.120546595	0.032258065
25	0.242764891	0.099328745
26	0.270950589	0.132853403

the laser repetition rate at a positive focal plane position effectively reduce the hole taper angle. Generally, a longer pulse duration results in a lower hole taper angle. This is because a longer pulse duration provides greater laser fluence per pulse, enhancing the penetration capability of the laser beam into the workpiece and effectively removing material from the lower section of the hole, resulting in a larger hole exit diameter. Regarding laser power, it is worth mentioning that increasing the power from 500 to 600 W shows a considerable decrease in the hole taper angle. However, there are no changes in the hole taper angle when the power is increased from 600 to 700 W. Therefore, a higher peak power primarily reduces the hole taper angle.

6.3 Inlet circularity

As can be seen from the ANOVA in Tables 16 and 17, the laser power, laser frequency, and duty cycle affect the inlet circularity significantly. In this case, neither interactions nor quadratic terms were significant. Equation 22 shows the

Fig. 21 Comparison between prediction models

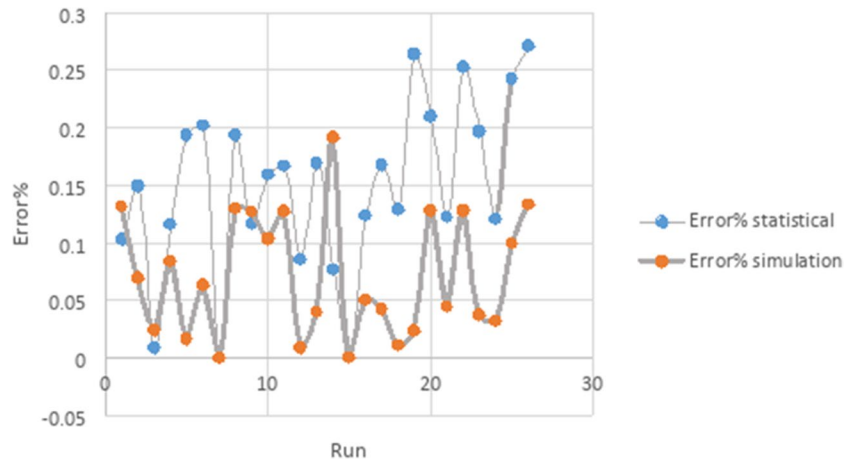


Table 20 Optimal setting

Response	Goal	Lower	Target	Upper	Weight	Importance
Inlet circularity	Maximum	0.584	0.904		1	1
<i>D</i> (in), mm	Target	550.000	600.000	650.000	1	3
Taper angle	Minimum		0.880	5	1	1

Table 21 Predicted result with optimal setting

Solution	<i>P</i>	<i>f</i>	<i>D</i>	<i>FPP</i>	Inlet circularity	<i>D</i> (in), mm	Taper angle	Composite desirability
1	631.820	20,000	42.0181	11.6275	0.832329	600	2.39415	0.920975

Table 22 Validation test

<i>P</i>	<i>f</i>	<i>D</i>	<i>FPP</i>	Inlet circularity	<i>D</i>	Hole taper angle
600	20,000	40	11.5	0.8	595	2.5

regression model with uncoded values for the hole taper angle considering significant parameters. The ANOVA of hole taper angle in Table 18 indicates that the regression model output fits it with a good estimation.

$$\text{Inlet circularity} = 1.2434 - 0.000405 P \text{ (W)} + 0.000005F \text{ (Hz)} - 0.006234 D \text{ (\%)} \tag{22}$$

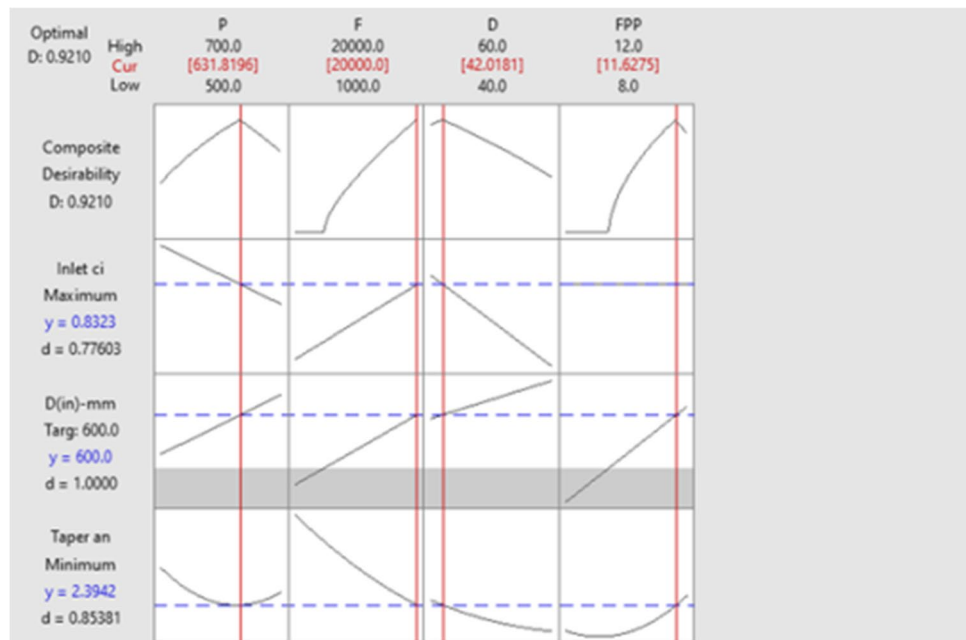
The surface and interaction plots are depicted in Figs. 19 and 20, respectively. In Figs. 19a and 20, it is observed that increasing the laser frequency and decreasing the duty cycle

Table 23 Optimization results

Response	Fit	<i>SE</i> fit	95% <i>CI</i>	95% <i>PI</i>
Inlet circularity	0.8323	0.0109	(0.8094, 0.8552)	(0.7717, 0.8929)
<i>D</i> (in), mm	600.0	17.3	(563.8, 636.2)	(507.8, 692.2)
Taper angle	2.39	1.10	(−0.20, 4.99)	(−1.40, 6.19)

lead to a shorter pulse width and a lower Feret ratio diameter, resulting in an improvement in the circularity of the hole. The pulse width, which is determined by the combination of the duty cycle and laser frequency, has a significant main effect on the hole circularity. Using a shorter pulse duration reduces the duration of melt ejection during each pulse, resulting in less variability in hole circularity and fewer burrs and debris during hole formation. In other words, by increasing the pulse frequency, the entrance hole diameter increases, because by increasing the pulse frequency, accumulation of heat is applied on the workpiece. Moreover, the highest inlet circularity is achieved at a laser frequency of 20,000 Hz and a duty cycle of 40%. Furthermore, Fig. 19b indicates that increasing the laser power results in more heat transmitted to the target material. This increased heat input leads to the expansion of the melted surface region in the radial direction, resulting in less circular holes. In

Fig. 22 Optimization graph



conclusion, it can be stated that shorter pulse widths, higher peak powers, and lower focal plane positions contribute to the formation of more circular holes. Notably, the results indicate that pulse frequency alone does not have a significant effect on hole circularity.

7 Comparison between the statistical model and simulation model

In this section, the comparison between the statistical model and the simulation model is assessed. For inlet hole diameter, with reference to simulation results and the ANOVA resultant model, deviation from experimental results is reported. As can be seen, the whole simulation error points are lower than statistical errors' points. It is concluded that the following simulation model is a better tool for predicting the laser beam percussion micro-drilling process. Simulation and statistical errors are reported in Table 19 and Fig. 21.

8 Desirability optimization

The aim of this research was to achieve the highest quality in the LBPMD process, which includes the correct inlet diameter, the lowest hole taper angle, and the highest inlet hole circularity. By statistically analyzing the results, regression equations establish an accurate relationship between input factors and output responses. Subsequently,

a multi-parameter optimization of the microsecond LBPMD process was conducted using the desirability optimization methodology to obtain the most desirable and high-quality hole. This methodology is based on Derringer's desirability function, where values closer to 1 indicate the ideal case for desirability [34–36]. Table 20 presents the output responses, criteria, and constraint factors, along with their respective importance. Given the high importance of precise inlet hole diameter, a value of 3 was assigned to $D(\text{in})$. The optimization criteria, as shown in Tables 21, 22, and 23 and Fig. 22, were determined by aiming for the minimum hole taper angle, the maximum hole circularity, and a target value for the hole entrance diameter. The experimental tests were conducted using the optimized predicted results to validate the statistical model. Table 22 provides the validation test results based on the suggested input parameters.

9 Conclusions

In this research, we used FEA with Abaqus to model heat conduction during microsecond LBPMD. This allowed us to predict the dimensions and temperature distribution during the drilling process. Our study is unique because it incorporates material removal using a mesh moving technique and accurately models microsecond laser percussion drilling. The modeling implementation includes two subroutines: UMESHMOTION for progressive shape change (material removal) through heat conduction and

DFLUX for generating heat. We conducted simulations using a 1-kW fiber laser with specific parameters for aerospace nickel-based superalloy Hastelloy X. Experimental tests were performed to validate the model, and the predicted hole dimensions aligned well with the experimental results. We then analyzed the effects of laser drilling parameters on the geometric features of the drilled holes. Regression equations were proposed to establish the relationship between input parameters and output responses. Finally, a multi-objective optimization was conducted to determine the optimal settings for achieving high-quality drilled holes. According to all experiments, the following results can be extracted:

- All input factors, laser power, laser frequency, focal plane position, and duty cycle, affect entrance hole diameter significantly. An increase in these factors leads to a bigger entrance hole.
- Increasing the laser frequency leads to significant reduction in heat conduction losses. This results in a greater accumulation of heat input transmitted to the material, leading to higher rates of ablation. It is important to note that the laser frequency has a considerable impact on the peak power of each pulse. If the repetition rate is too high, the peak power drops substantially after the first pulse, preventing successful drilling of the target material. On the other hand, a notable observation is that when two adjacent pulses are irradiated on the target for a specific duration, there is a collaborative effect that causes the melted material to solidify. As a result, blockages form in the drilled hole.
- All the parameters, except laser power, have significant effects on the hole taper angle. A higher focal plane position can result in a larger outlet hole diameter, leading to a higher hole taper angle. The interaction between duty cycle (D) and laser frequency (f) is highly significant. A longer pulse duration results in a lower hole taper angle. This is because longer pulses provide greater laser fluence, improving the laser beam's ability to penetrate the workpiece and effectively remove material at the lower section of the hole, resulting in a larger hole exit diameter.
- The laser power, laser frequency, and duty cycle affect the inlet circularity significantly. An increase in laser frequency and a decrease in duty cycle result in a shorter pulse width and a lower Feret ratio diameter, i.e., an elevation in the circularity of the hole. Pulse width, which is considered a combination of the duty cycle and laser frequency parameters, has the remarkable main effect on hole circularity, whereby using a shorter pulse duration would reduce the duration of melt ejection during each pulse.
- Assessments indicate that the recommended simulation model is more adequate than the statistical model to predict the inlet hole diameter of a laser beam percussion micro-drilled hole.

Data availability All data will be provided upon request from the corresponding author.

Declarations

Ethics approval Not applicable.

Consent to participate Not applicable.

Consent for publication All authors read and approved the final manuscript for publication.

Competing interests The authors declare no competing interests.

Open Access This article is licensed under a Creative Commons Attribution 4.0 International License, which permits use, sharing, adaptation, distribution and reproduction in any medium or format, as long as you give appropriate credit to the original author(s) and the source, provide a link to the Creative Commons licence, and indicate if changes were made. The images or other third party material in this article are included in the article's Creative Commons licence, unless indicated otherwise in a credit line to the material. If material is not included in the article's Creative Commons licence and your intended use is not permitted by statutory regulation or exceeds the permitted use, you will need to obtain permission directly from the copyright holder. To view a copy of this licence, visit <http://creativecommons.org/licenses/by/4.0/>.

References

1. Yu ZY, Zhang Y, Li J, Luan J, Zhao F, Guo D (2009) High aspect ratio micro-hole drilling aided with ultrasonic vibration and planetary movement of electrode by micro-EDM. *CIRP Ann* 58(1):213–216. <https://doi.org/10.1016/J.CIRP.2009.03.111>
2. Ferraris E, Castiglioni V, Ceysens F, Annoni M, Lauwers B, Reynaerts D (2013) EDM drilling of ultra-high aspect ratio micro holes with insulated tools. *CIRP Ann* 62(1):191–194. <https://doi.org/10.1016/J.CIRP.2013.03.115>
3. Pattanayak S, Panda S, Dhupal D (2020) Laser micro drilling of 316L stainless steel orthopedic implant : a study. *J Manuf Process* 52(January):220–234. <https://doi.org/10.1016/j.jmapro.2020.01.042>
4. B Guo et al. (2021) Origins of the mechanical property heterogeneity in a hybrid additive manufactured Hastelloy X, *Mater Sci Eng A*, 823, 141716. <https://doi.org/10.1016/J.MSEA.2021.141716>.
5. Xu L, Gao Y, Zhao L, Han Y, Jing H (2022) Ultrasonic micro-forging post-treatment assisted laser directed energy deposition approach to manufacture high-strength Hastelloy X superalloy. *J Mater Process Technol* 299:117324. <https://doi.org/10.1016/J.JMATPROTEC.2021.117324>
6. Azimzadegan T, Akbari Mousavi SAA (2019) Investigation of the occurrence of hot cracking in pulsed Nd-YAG laser welding of Hastelloy-X by numerical and microstructure studies. *J*

- Manuf Process 44:226–240. <https://doi.org/10.1016/J.JMAPRO.2019.06.005>
7. Zahra WK, Abdel-Aty M, Abidou D (2020) A fractional model for estimating the hole geometry in the laser drilling process of thin metal sheets. *Chaos, Solitons Fractals* 136:109843. <https://doi.org/10.1016/J.CHAOS.2020.109843>
 8. He C, Zibner F, Fornaroli C, Ryll J, Holtkamp J, Gillner A (2014) High-precision helical cutting using ultra-short laser pulses. *Phys Procedia* 56(C):1066–1072. <https://doi.org/10.1016/J.PHPRO.2014.08.019>
 9. Zhang H, Di J, Zhou M, Yan Y, Wang R (2015) An investigation on the hole quality during picosecond laser helical drilling of stainless steel 304. *Appl Phys A Mater Sci Process* 119(2):745–752. <https://doi.org/10.1007/s00339-015-9023-5>
 10. Ghoreishi M, Nakhjavani OB (2008) Optimisation of effective factors in geometrical specifications of laser percussion drilled holes. *J Mater Process Technol* 196(1–3):303–310. <https://doi.org/10.1016/J.JMATPROTEC.2007.05.057>
 11. Iwatani N, Doan HD, Fushinobu K (2014) Optimization of near-infrared laser drilling of silicon carbide under water. *Int J Heat Mass Transf* 71:515–520. <https://doi.org/10.1016/J.IJHEATMASS TRANSFER.2013.12.046>
 12. Romoli L, Vallini R (2016) Experimental study on the development of a micro-drilling cycle using ultrashort laser pulses. *Opt Lasers Eng* 78:121–131. <https://doi.org/10.1016/J.OPTLASENG.2015.10.010>
 13. Ho C-C, Chen Y-M, Hsu J-C, Chang Y-J, Kuo C-L (2015) Characteristics of the effect of swirling gas jet assisted laser percussion drilling based on machine vision. *J Laser Appl* 27(4):042001. <https://doi.org/10.2351/1.4923019>
 14. Moradi M, Abdollahi H (2018) Statistical modelling and optimization of the laser percussion microdrilling of thin sheet stainless steel. *Lasers Eng* 40(4–6):375–393
 15. Saravanan M, Bupesh Raja VK, Palanikumar K, Vaidyaa P, Sundar S, Surya Prakash M (2020) Laser drilling parameter optimization for Ti6Al4v alloy. *Mater Today Proc* 46:4003–4007. <https://doi.org/10.1016/j.matpr.2021.02.538>
 16. Liu C, Zhang X, Gao L, Jiang X, Li C, Yang T (2021) Feasibility of micro-hole machining in fiber laser trepan drilling of 2.5D Cf/SiC composite: experimental investigation and optimization. *Optik (Stuttg)* 242:167186. <https://doi.org/10.1016/J.IJLEO.2021.167186>
 17. Nasrollahi V, Penchev P, Jwad T, Dimov S, Kim K, Im C (2018) Drilling of micron-scale high aspect ratio holes with ultra-short pulsed lasers: critical effects of focusing lenses and fluence on the resulting holes' morphology. *Opt Lasers Eng* 110(January):315–322. <https://doi.org/10.1016/j.optlaseng.2018.04.024>
 18. Moradi M, Golchin E (2017) Investigation on the effects of process parameters on laser percussion drilling using finite element methodology; statistical modelling and optimization. *Lat Am J Solids Struct* 14(3):464–484. <https://doi.org/10.1590/1679-78253247>
 19. Panda S, Mishra D, Biswal BB (2011) Determination of optimum parameters with multi-performance characteristics in laser drilling—a grey relational analysis approach. *Int J Adv Manuf Technol* 54(9–12):957–967. <https://doi.org/10.1007/s00170-010-2985-8>
 20. Zhao W, Shen X, Liu H, Wang L, Jiang H (2020) Effect of high repetition rate on dimension and morphology of micro-hole drilled in metals by picosecond ultra-short pulse laser. *Opt Lasers Eng* 124:105811. <https://doi.org/10.1016/j.optlaseng.2019.105811>
 21. Sattarpanah Karganroudi S et al (2021) Experimental and numerical analysis on TIG arc welding of stainless steel using RSM approach. *Metals* 11(10):1659. <https://doi.org/10.3390/met11101659>
 22. Alzaydi A (2018) Trajectory generation and optimization for five-axis on-the-fly laser drilling: a state-of-the-art review. *Opt Eng* 57(12). <https://doi.org/10.1117/1.OE.57.12.120901>
 23. Moradi M, Hasani A, Pourmand Z, Lawrence J (2021) Direct laser metal deposition additive manufacturing of Inconel 718 superalloy: statistical modelling and optimization by design of experiments. *Opt Laser Technol* 144:107380. <https://doi.org/10.1016/J.OPTLASTEC.2021.107380>
 24. Moradi M, MohazabPak AR (2018) Statistical modelling and optimization of laser percussion microdrilling of Inconel 718 sheet using response surface methodology (RSM). *Lasers Eng* 39(3–6):313–331
 25. Ghoreishi M (2006) Statistical analysis of repeatability in laser percussion drilling. *Int J Adv Manuf Technol* 29(1–2):70–78. <https://doi.org/10.1007/s00170-004-2489-5>
 26. Aghaee Attar M, Ghoreishi M, Malekshahi Beiranvand Z (2020) Prediction of weld geometry, temperature contour and strain distribution in disk laser welding of dissimilar joining between copper & 304 stainless steel. *Optik (Stuttg)* 219:165288. <https://doi.org/10.1016/J.IJLEO.2020.165288>
 27. Lee D, Kannatey-Asibu E (2009) Numerical analysis of ultra-short pulse laser-material interaction using ABAQUS. *J Manuf Sci Eng Trans ASME* 131(2):0210051–02100515. <https://doi.org/10.1115/1.3075869>
 28. Afrasiabi M, Wegener K (2020) 3D thermal simulation of a laser drilling process with meshfree methods. *J Manuf Mater Process* 4(2):1–20. <https://doi.org/10.3390/JMMP4020058>
 29. Mishra S, Yadava V (2013) Modeling and optimization of laser beam percussion drilling of nickel-based superalloy sheet using Nd: YAG laser. *Opt Lasers Eng* 51(6):681–695. <https://doi.org/10.1016/j.optlaseng.2013.01.006>
 30. Zhang J, Zong X, Chen Z, Fu H (2021) A numerical simulation and process optimization of a Hastelloy X alloy single track produced by selective laser melting. *Trans Indian Inst Metals*. <https://doi.org/10.1007/s12666-021-02407-2>
 31. Vasantgadkar NA, Bhandarkar UV, Joshi SS (2010) A finite element model to predict the ablation depth in pulsed laser ablation. *Thin Solid Films* 519(4):1421–1430. <https://doi.org/10.1016/J.TSF.2010.09.016>
 32. Fu CH, Sealy MP, Guo YB, Wei XT (2015) Finite element simulation and experimental validation of pulsed laser cutting of nitinol. *J Manuf Process* 19:81–86. <https://doi.org/10.1016/j.jmapro.2015.06.005>
 33. Tu JF, Lehman T, Reeves N (2016) Rapid and high aspect ratio micro-hole drilling with multiple micro-second pulses using a CW single-mode fiber laser. *High Speed Mach* 2(1):26–36. <https://doi.org/10.1515/hsm-2016-0003>
 34. Moradi M, Fallah MM (2018) Multi-response optimization of CO2 laser welding of Rene 80 using response surface methodology (RSM) and the desirability approach. *Int J Laser Sci: Fundamental Theory Analytical Methods* 1(3–4):265–277
 35. Derringer G, Suich R (1980) Simultaneous optimization of several response variables. *J Qual Technol* 12(4):214–219
 36. Fallah MM, Attar MA, Mohammadpour A, Moradi M, Barka N (2021) Modelling and optimizing surface roughness and MRR in electropolishing of AISI 4340 low alloy steel in eco-friendly NaCl based electrolyte using RSM. *Mater Res Exp* 8(10):106528

Publisher's Note Springer Nature remains neutral with regard to jurisdictional claims in published maps and institutional affiliations.